Progress In Electromagnetics Research, Vol. 140, 181–197, 2013

ESTIMATING THE REDUCTION OF RADIATED EMISSIONS FROM TFT-LCD PANEL USING NETWORK ANALYZER WITH A BULK CURRENT INJECTION PROBE

Cheng-Yu Ho[1, *], Kai-Syuan Chen[1], Tzyy-Sheng Horng[1], and Jian-Ming Wu[2]

[1]Department of Electrical Engineering, National Sun Yat-Sen University, No. 70, Lien-Hai Rd., Kaohsiung 804, Taiwan

[2]Department of Electronic Engineering, National Kaohsiung Normal University, Kaohsiung 824, Taiwan

Abstract—A network analyzer with a bulk current injection (BCI) probe is proposed to measure the common-mode conversion coefficient for DC supply loops on a driver PCB of thin film transistor-liquid crystal display (TFT-LCD) panel. The proposed technique is used to predict the common-mode radiated emission caused by the DC supply loops, which highly correlates with the radiated emission measurements obtained for the TFT-LCD panel in a fully anechoic chamber (FAC). The proposed technique is also successful to estimate the reduction of a specific peak in the radiated emission spectrum by shielding the DC supply loops on a driver PCB of TFT-LCD panel. Electromagnetic simulation and equivalent-circuit modeling approaches are developed to confirm the common-mode radiation mechanism in this study.

1. INTRODUCTION

Radiated emissions from printed circuit boards (PCBs) are very complex and difficult to resolve. The main problem is the lack of reliable and convenient methods for analyzing and predicting PCB radiation. Until now, therefore, methods of diagnosing and solving problems of PCB radiated emissions have mainly relied on experimental techniques [1–3]. The difficulty in methods of predicting PCB radiated emissions by simulation is the combination of circuit and electromagnetic models of practical interactions between

---

Received 11 April 2013, Accepted 8 May 2013, Scheduled 29 May 2013

* Corresponding author: Cheng-Yu Ho (d943010018@student.nsysu.edu.tw).

integrated circuits and PCB traces [4]. Far-field radiated emissions can be measured in a fully anechoic chamber to obtain the spectra needed to evaluate conformity to electromagnetic compatibility (EMC) regulations [5–8]. However, performing far-field measurements is very costly and time-consuming. Another common method of measuring PCB radiated emissions is to use a magnetic or electric field probe for near-field scanning of the PCB surface [9–13]. Although the associated test setup and procedure are simpler than those for far-field measurement, the near-field scan results are more effective for locating the source of radiated emission than for predicting radiated emission levels as required by EMC specifications.

In recent years, the network analyzer measurements have been used in EMC application to measure S-parameters, which correlate with the electromagnetic emission and susceptibility. Recent applications of network analyzer include measurements of S-parameters used to elucidate radiation mechanisms by describing the conversion from differential to common mode [14, 15], and measurements of the transfer function of the coupling path that correlates with conducted susceptibility [16]. By coupling external disturbance to harness, bulk current injection (BCI) probes have also proven effective for simulating radiation-induced effects in conducted susceptibility tests [17].

The authors' previous work [18, 19] presented a method of measuring the common-mode conversion coefficient by using a VNA and a BCI probe to characterize the common-mode radiation from a PCB with an area of up to several tens of square centimeters. As a practical application, the proposed technique is extended to determine radiated emission from a driver PCB in a TFT-LCD panel and to predict the improved radiated emission obtained by adding a shielding foil. By associated modeling approaches, our proposed method can predict effectively the PCB radiated emissions and estimate accurately the radiated emissions reduction.

2. CALIBRATION AND MODELING OF BCI PROBE

In this work, a BCI probe was used to measure common-mode current on a PCB. To measure common-mode current on a PCB, the BCI probe must be calibrated to determine the transfer impedance [17]. Note that the BCI probe used in this study was manufactured by Fischer Custom Communication (FCC) with a model number F-130-1A [20]. It is designed for operating frequencies between 50 and 400 MHz. Therefore, the proposed techniques carry out calibration and measurement in the same frequency range. Fig. 1 shows the experimental setup for measuring the transfer impedance of the BCI

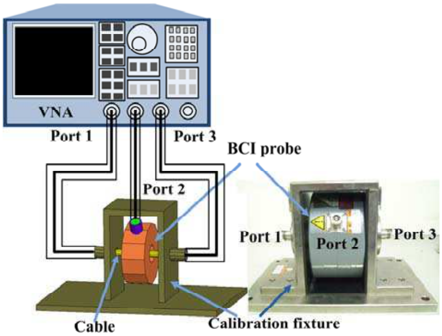

Figure 1. Experimental setup for measuring transfer impedance of BCI probe using calibration fixture.

probe. The default calibration procedure is performed with the BCI probe mounted on a calibration fixture. The transfer impedance of a BCI probe is measured under a specified load of 50 Ω. Fig. 1 shows that port 1 of a VNA is connected to the input port of the calibration fixture, port 2 is connected to the BCI probe and port 3 is connected to the output port of the calibration fixture. The excitation of the input port generates currents in the cable of the calibration fixture and induces a voltage on the BCI probe. By definition, the transfer impedance relates the current in the cable of the calibration fixture to the voltage at the BCI probe output. The transfer impedance of the BCI probe is given by

$$Z_T(\omega) = \frac{V_2}{I_1} = \left(\frac{V_1}{I_1}\right) \cdot \left(\frac{V_2}{V_1}\right) = 50 \cdot S_{21,fixture}(\omega) \tag{1}$$

where V_2 is the output voltage of BCI probe loaded with $50\,\Omega$, I_1 the current that is flowing in the coaxial line of calibration fixture, and V_1 the incident voltage to the coaxial line of calibration fixture. In this formula, the magnitude transfer impedance $Z_T(\omega)$ is obtained in dBΩ from the S-parameter $S_{21,fixture}(\omega)$, which can be measured in the calibration procedure. The BCI probe in this study had a transfer impedance of about 28 dBΩ in the frequency range 50 MHz–400 MHz.

Regarding the modeling and EM simulation of the BCI probe, an equivalent-circuit model of the BCI probe was obtained by measuring the input impedance $Z_{in}(\omega)$ of the BCI probe with the calibration fixture removed. Fig. 2(a) presents the geometrical configuration of the BCI probe and Fig. 2(b) depicts the corresponding equivalent-circuit model. The BCI probe is consisting of a metallic frame, a toroidal ferrite core, an inner winding and an input connector. The inner winding and metallic frame are considered perfect electric conductors

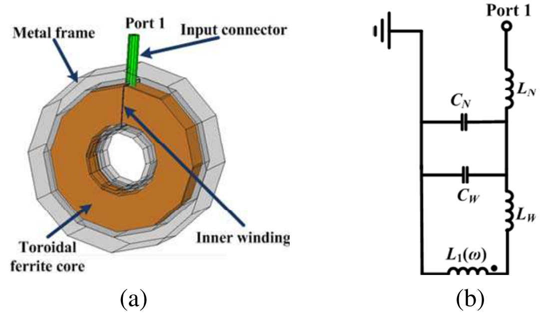

(a) (b)

Figure 2. (a) Geometrical configuration. (b) Equivalent circuit model of the BCI probe. ($L_N \approx 3\,\mathrm{nH}$, $C_N \approx 4\,\mathrm{pF}$, $L_W = 70\,\mathrm{nH}$, $C_W = 4\,\mathrm{pF}$).

while the toroidal ferrite core has a complex permeability given by the following Debye model [17].

In the equivalent-circuit model of the BCI probe, the toroidal ferrite core has complex permeability. To obtain the frequency-dependent and lossy characteristics of the toroidal ferrite core of the BCI probe, the reflection coefficient measured by the VNA is converted to the input impedance of the BCI probe. Parameters L_N and C_N in the input impedance equation used to model the effects of the input connector are estimated according to the physical dimensions and material properties of the BCI probe. Parameters L_W and C_W denote the total capacitance and inductance, respectively, between the inner winding and the metallic frame. These parameters can be

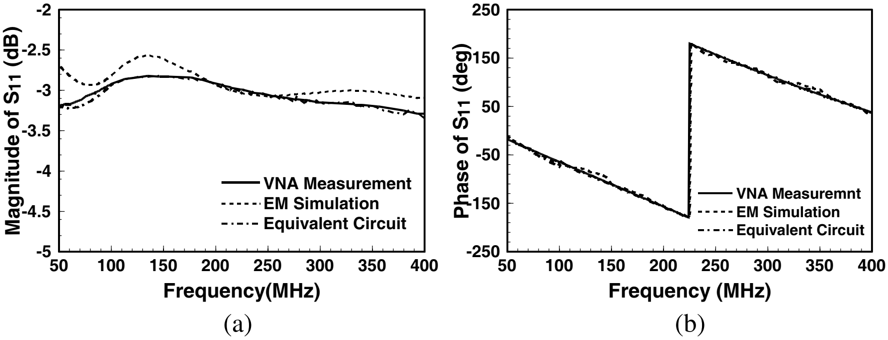

(a) (b)

Figure 3. Comparison of S_{11} among VNA measurement, EM simulation and equivalent circuit model of the BCI probe. (a) Magnitude of S_{11}. (b) Phase of S_{11}.

evaluated by considering the case of a single wire above a ground plane made by the metallic frame. Parameter $L_1(\omega)$ represents the complex and frequency-dependent self inductance of the primary winding of the probe. More detailed modeling information for the BCI probes can refer to [17, 19]. Figs. 3(a) and 3(b) present the magnitude and phase of the input reflection coefficient of the BCI probe, respectively. The EM simulation and equivalent-circuit model are consistent with the measurements obtained at 50–400 MHz.

3. DIAGNOSIS OF COMMON-MODE RADIATION FROM TFT-LCD PANEL

3.1. Radiated Emission Problem in a TFT-LCD Panel

The radiated emission from TFT-LCD panel was measured by a VNA with BCI probe. Empirically, the main contributor to radiated emission is the driver PCB of TFT-LCD panel. The driver PCB consists mainly of a timing controller (T-CON), a source driver IC and a DC-to-DC converter, as shown in Fig. 4. According to experimental data in [21], most EMI noise sources of TFT-LCD panel come from the T-CON and occur at the clock harmonic frequencies. Fig. 4(a) shows that the DC-to-DC converter provides DC power to the source driver IC via a DC supply loop. Fig. 4(b) shows a corresponding photograph. The driver PCB has a size of 35 cm × 5 cm. Because the clock signal generated by T-CON was coupled to the DC supply loop, a decoupling capacitor was needed.

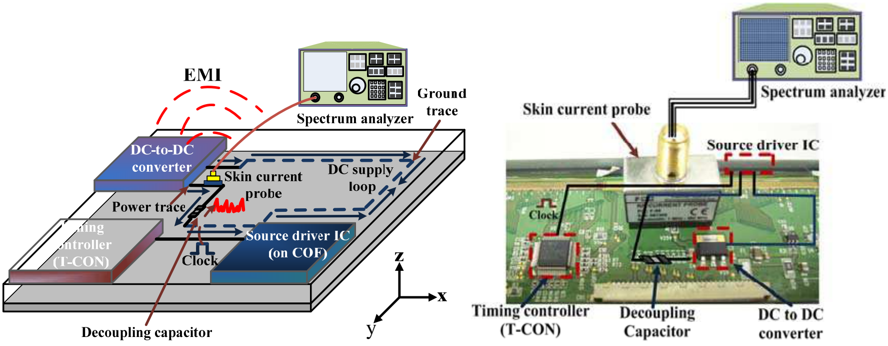

(a) (b)

Figure 4. Detection of noise source on the TFT-LCD driver PCB for radiated emission generation. (a) Illustration of measurement method. (b) Corresponding photograph of (a).

In the radiation mechanism of the TFT-LCD panel, the T-CON may be a major EMI source and the DC supply loop may be a major radiator. This inference was tested by using a biconical-log-periodic antenna and a spectrum analyzer with an amplifier as a receiver to measure TFT-LCD panel emissions in a fully anechoic chamber (50 MHz to 1 GHz).

The TFT-LCD panel was 3 m away from the receiving biconical-log-periodic antenna. At each frequency, the maximum far-field radiated emission was determined using measurements obtained by horizontally and vertically polarized antennas. Fig. 5 presents radiated emission from the TFT-LCD panel. Notably, the peaks of radiated emission from the TFT-LCD panel were clearly visible at 140 MHz, 210 MHz and 280 MHz, which were in the second to fourth harmonics, respectively, of the clock signal from T-CON. The Federal Communications Commission (FCC) Class B limit is 43.5 dBuV/m from 88 to 216 MHz and 46 dBuV/m from 216 to 960 MHz. Fig. 5 shows that the peak emission radiated from the TFT-LCD panel at 140 MHz was approximately 38 dBuV/m, which closely approximates the FCC Class B limit. Therefore, radiated emission from the TFT-LCD panel is responsible only for the peak at 140 MHz. The other peaks are not considered because they do not approach the limit.

The radiation energy of clock signal is concentrated at the fundamental and harmonic frequencies. To reduce radiated emission from a TFT-LCD panel, spread-spectrum clocking (SSC) approaches are widely used [22]. These SSC techniques reduce the peak radiated emission by spreading the frequency component of the clock signal from T-CON. As noted above, the clock signal from T-CON couples to the DC supply loop. This finding was confirmed by using a spectrum

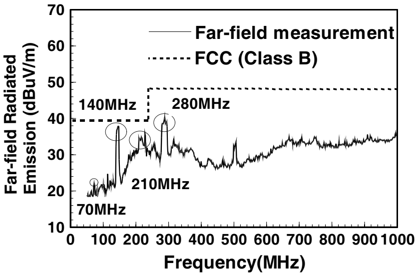

Figure 5. Far-field radiated emission from TFT-LCD panel obtained in a fully anechoic chamber.

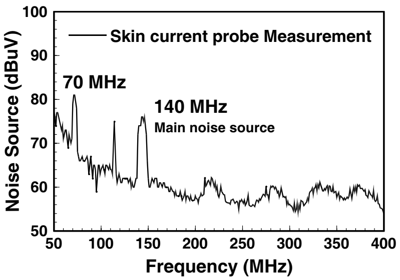

Figure 6. Measured spectrum of noise coupled from T-CON to DC-supply loop.

analyzer and a skin current probe to measure the noise spectrum on the loop. Fig. 4(a) shows that the skin current probe was placed around the power trace of DC supply loop between the DC-to-DC converter and the source driver IC. Fig. 6 presents the measured spectrum results. The noise peaks at 70 and 140 MHz result from the fundamental and second harmonics of the SSC signal. Although the noise peaks were reduced by SSC technique, the radiated emission at 140 MHz in the far field still approached the FCC Class B limit.

3.2. Common-mode Current on a DC Supply Loop

A literature review shows that radiated emissions from TFT-LCD panel have diverse ways [23–26]. The DC supply loop is one of the major radiation mechanisms because it may behave like an antenna, radiating the noises that were coupled from the T-CON. Empirically, the radiation from a DC supply loop is maximal when resonance occurs. This study therefore characterized the effect of resonance by using a VNA to measure the input impedance of the DC supply loop. Fig. 7(a) shows that the DC supply loop on the driver PCB is duplicated on another PCB with an area of $20 \times 10\,\mathrm{mm}^2$ and then connected to a VNA via an SMA connector. Fig. 7(b) is a photograph showing the physical dimensions of the duplicated DC supply loop. Fig. 8 plots the real and imaginary parts, respectively, of the input impedance at a frequency of 50 to 400 MHz. The measurement results clearly demonstrate that the duplicated DC supply loop resonates at 140 MHz. After the parasitic elements of the metallic loop and the 100-nF decoupling capacitor were extracted from Ansys-Ansoft Q3D

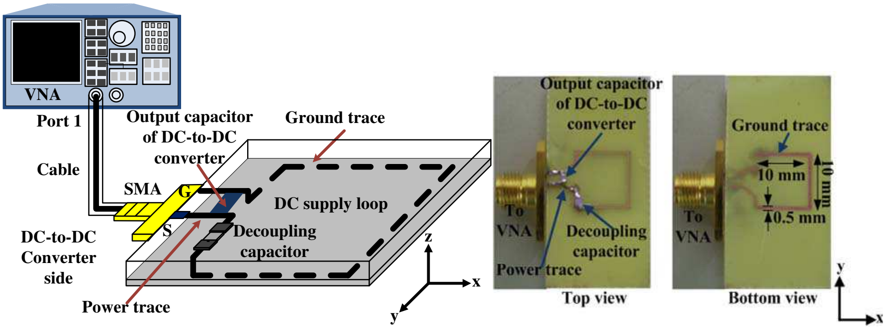

(a) (b)

Figure 7. On-PCB DC supply loop connected to VNA to measure its input impedance. (a) Measurement setup. (b) Photograph and physical dimensions of the DC supply loop.

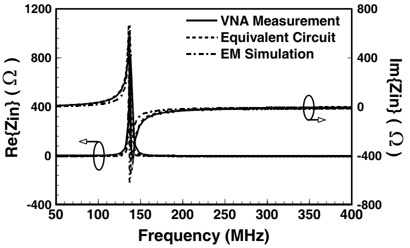

Figure 8. Comparison of input impedance of the DC supply loop among VNA measurement, EM simulation and equivalent-circuit model.

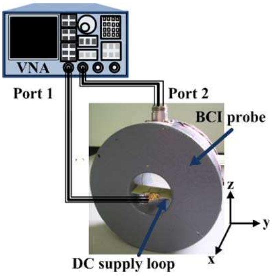

Figure 9. Corresponding photograph of experimental setup for measuring common-mode conversion coefficient of the DC supply loop.

and VNA measurement, respectively, the equivalent circuit of the DC supply loop was established in Fig. 10 to confirm the measured input impedance response, as shown in Fig. 7. The experimental results thus far show that the second harmonic frequency of the clock signal is extremely close to that of the self-resonance of the DC supply loop, which is a frequency at which significant radiation is generated. Fig. 4(a) shows the clock signal from T-CON couples to the DC supply loop between the DC-to-DC converter and the source driver IC.

The signal excites the common- and differential-mode currents on the loop. Theoretically, the common-mode current generates much more radiation compared to the differential-mode current. Therefore, the common-mode current is the dominant source of radiated emission from the driver PCB of TFT-LCD panel. Notably, the perimeter of the DC supply loop is only about a twentieth of a wavelength at 140 MHz. Therefore, since the DC supply loop is inefficient for a radiating loop antenna at 140 MHz, the associated radiation effects were not considered in this study.

In this work, a VNA with a BCI probe was used to measure the common-mode current on the DC supply loop. According to the Ampere's circuital law, the x-directed currents should induce the magnetic field around x-axis and the y-directed currents should induce the magnetic field around y-axis. Therefore, the BCI probe oriented perpendicularly to the x-axis of the Cartesian coordinates should measure the magnetic field induced by the x-directed currents. Similarly, a BCI probe oriented perpendicularly to the y-axis of the Cartesian coordinates should measure the magnetic field induced by the y-directed currents. In this case, however, the excitation of common-mode currents on the DC supply loop produces the in-phase x-directed components and out-of-phase y-directed components between the power trace and the ground trace. Therefore, the x-directed components dominate the common-mode currents on the DC supply loop. For this reason, the BCI probe measures only the magnetic field induced by the x-directed common-mode currents. Fig. 9 shows the experimental setup for measuring the common-mode conversion coefficient of the same DC supply loop as measured earlier by VNA to obtain the input impedance.

A two-port measurement configuration is used in which one port of the VNA is connected to the DC supply loop on the PCB inserted into the center hole of the BCI probe, and the other port of the VNA is connected to the BCI probe. Fig. 10 shows an equivalent-circuit model corresponding to the experimental setup in Fig. 9. Both the power and ground traces are much shorter than one wavelength and each can be represented by an equivalent inductance. Because of the different lengths of power and ground traces, the differential-mode current that flows through the power and ground traces causes different voltage drops across the equivalent inductances, which are regarded as the source of common-mode current generation. Notably, in Fig. 10, Parameters C_{dec}, L_e, and R_e are used to model the decoupling capacitor with values 100 nF, 0.479 nH, and 0.063 Ω, respectively, from the component datasheet. Parameter C_{out} represents the output capacitance of DC-to-DC converter and its value can be estimated

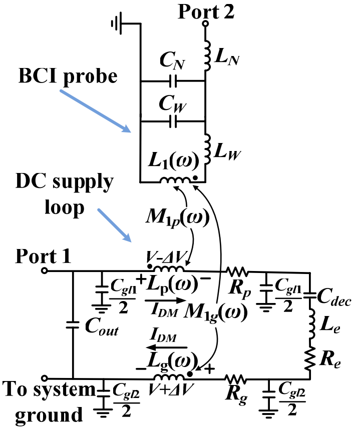

Figure 10. Corresponding equivalent-circuit model of experimental setup for measuring common-mode conversion coefficient of the DC supply loop. ($L_p = 4\,\text{nH}$, $R_p = 0.01\,\Omega$, $L_g = 23\,\text{nH}$, $R_g = 0.07\,\Omega$, $C_{g11} = 0.01\,\text{pF}$, $C_{g12} = 0.064\,\text{pF}$, $C_{out} = 48\,\text{pF}$, $C_{dec} = 100\,\text{nF}$, $L_e = 0.479\,\text{nH}$, $R_e = 0.063\,\Omega$).

using the resonant frequency of DC supply loop as 48 pF. Parameters L_p, R_p, L_g, and R_g are model elements for the DC supply loop and their values were extracted from Ansys-Ansoft Q3D as 4 nH, 0.01 Ω, 23 nH, and 0.07 Ω, respectively. Parameters C_{gl1} and C_{gl2}, the shunt capacitances from the power and ground traces, respectively, to the metallic frame of the BCI probe, were obtained as the coaxial-line capacitances. The clamped conductor was considered as signal wire, and the inner surface of the probe metallic frame was considered as reference conductor. A simple formula is used to calculate the associated stray capacitance as follows.

$$C_{gl} = \frac{2\pi\varepsilon_0}{\ln\left(\frac{r_o}{r_i}\right)} l_{probe} \quad \text{(F/m)} \tag{2}$$

where r_i denotes the radius of the clamped conductor, r_o the inner radius of the probe metallic frame, and l_{probe} the probe thickness.

Parameters $M_{1p}(\omega)$ and $M_{1g}(\omega)$ represent the mutual inductances between the inner winding of the BCI probe and the metal traces of DC supply loop. The mutual inductance $M_{1p}(\omega)$ and $M_{1g}(\omega)$ take the expressions: $M_{1p}(\omega) = M_{1g}(\omega) = L_1(\omega)/N_1$, where N_1 denotes the number of turns of the inner winding. Parameters k_{1p} and k_{1g} are the magnetic coupling coefficient, and they can be estimated using [17]

$$k_{1p} = \frac{M_{1p}(\omega)}{\sqrt{L_1(\omega) L_p}} \tag{3}$$

$$k_{1g} = \frac{M_{1g}(\omega)}{\sqrt{L_1(\omega) L_g}} \tag{4}$$

Figure 11 compares the common-mode conversion coefficients for the loop, which were obtained by measurement, EM simulation and

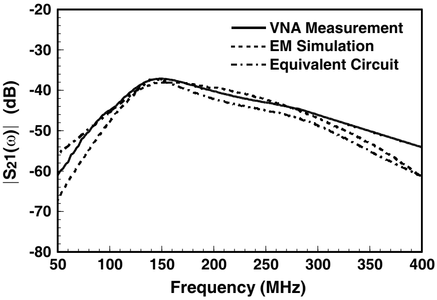

Figure 11. Comparison of common-mode conversion coefficient magnitude of the DC supply loop among VNA measurement, EM simulation and equivalent-circuit model.

application of an equivalent-circuit model. All results agreed well in the frequency range 50–400 MHz. Fig. 11 indicates that the peak magnitude occurs at 140 MHz, which is the resonant frequency of the DC supply loop.

The common-mode conversion coefficient $S_{21}(\omega)$ was further used to determine the common-mode current on DC supply loop as follows.

$$I_{CM}(\omega) = |V_{BCI}(\omega)/Z_T(\omega)| = |S_{21}(\omega)V_{inc}(\omega)/Z_T(\omega)| \tag{5}$$

where $V_{BCI}(\omega)$ is the induced voltage on the BCI probe, $V_{inc}(\omega)$ the incident voltage to the DC supply loop, and $Z_T(\omega)$ the transfer impedance of the BCI probe. Notably, $V_{BCI}(\omega)$ is the output voltage of port 2; $V_{inc}(\omega)$ is in practice estimated from the input continuous-wave signal, and $Z_T(\omega)$ as given by (1) is obtained from a default calibration procedure of the BCI probe.

3.3. Radiated Emission from a Driver PCB

A Hertzian dipole model demonstrates that the far-field radiated emission due to the common-mode current is given by [27–29]

$$E_{C_{\max}}(\omega) = 6.28 \times 10^{-7} \frac{I_{CM}(\omega) \cdot L \cdot \omega}{2\pi R} \tag{6}$$

where L is the length of the trace and R the distance between the measurement point and the PCB.

The far-field radiated emission from the DC supply loop on PCB was measured in a FAC. A signal generator provided a 0 dBm input to the DC supply loop with a frequency sweep of 50 to 400 MHz. The PCB was oriented horizontally 1 m above the ground plane of the chamber and 1 m away from the receiving biconical-log-periodic antenna. The power that was received from the antenna was detected using a spectrum analyzer. Fig. 12 compares the far-field radiated emissions measured in the FAC when predictions are made using (6) and full-wave simulation. All results agree well throughout the measurement frequency range. The radiation was maximal at 140 MHz when the DC supply loop was at resonance.

The driver PCB of the TFT-LCD panel has 24 DC supply loops of similar area. To simplify the calculation, each DC supply loop is assumed to produce the same radiation. Therefore, the estimated far-field radiated emission from the TFT-LCD panel is 24 times the radiated emission of a single loop. Based on (5) and (6), the VNA with a BCI probe can be used to predict the common-mode radiation from a single loop. In this study, the absolute value of $V_{inc}(\omega)$ in (5) was obtained from the measured spectrum of the clock signal coupled to the DC supply loop (Fig. 6). Fig. 13 compares the radiated emissions

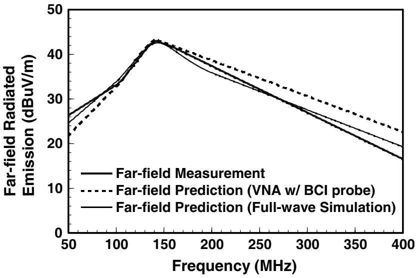

Figure 12. Comparison of far-field radiated emissions from the DC supply loop obtained in FAC with predictions based on VNA measurement and full-wave simulation.

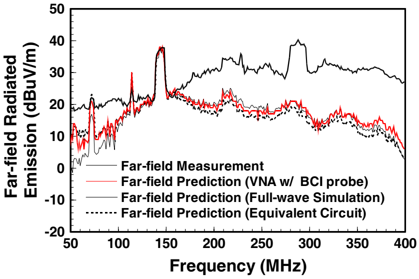

Figure 13. Comparison of radiated emission from TFT-LCD panel obtained in FAC with predictions based on VNA measurement, full-wave simulation and equivalent-circuit model.

measured in the FAC when (6) and full-wave simulation were used for making predictions. The solid line represents the radiated emissions that were measured in the FAC. The solid line (red) represents the radiated emissions that are determined using the VNA with a BCI probe. The thin solid line represents the radiated emissions that are determined using full-wave simulation. The dotted line represents the radiated emissions that are determined using equivalent-circuit model. Notably, the PCB driver board of the TFT-LCD panel has 24 DC supply loop and each has a different loop area. To simplify the calculation, each DC supply loop is assumed to produce the same radiation. Although radiated emissions from predictions are smaller than those from far-field measurement at higher frequency, the comparison reveals strong agreement for the peak at 140 MHz.

4. IMPROVEMENT AND ASSESSMENT METHODS

As discussed in the last section, the radiated emission at 140 MHz almost exceeds the FCC Class B limit. This work therefore employs a very simple and effective method of improving radiated emission without changing the original circuit structure on the driver PCB of the TFT-LCD panel. Moreover, the proposed measurement technique of using a VNA and a BCI probe can also be used to estimate the reduction of radiated emission. This improvement method places a shielding foil above and very close to each DC supply loop on the driver PCB of the TFT-LCD panel. The shielding foil is connected to the grounded chassis of TFT-LCD panel. Fig. 14 shows how a

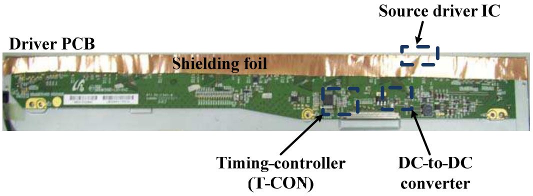

Figure 14. Use of shielding in the driver PCB to reduce the radiated emission from TFT-LCD panel.

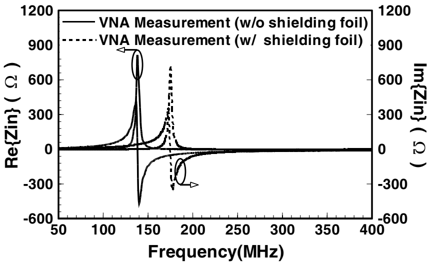

Figure 15. Comparison of measured input impedance of the DC supply loop between with and without shielding foil.

piece of shielding foil (2 cm × 35 cm) is used to cover the top of all DC supply loops on the driver PCB of the TFT-LCD panel Notably, the driver PCB is a two-layer board with the power traces on one side and the ground trace on the other side. The foil is very close to the all DC supply loops on the driver PCB of the TFT-LCD panel. The measurement results obtained with and without the improvement method, respectively. Fig. 15 shows that the resonant frequency of the DC supply loop shifted to 180 MHz when the improvement method was applied, and Fig. 16 compares the common-mode conversion coefficients for the loop obtained by measurement, full-wave simulation and application of an equivalent-circuit model. All results agreed well at 50–400 MHz. Fig. 16 shows that the magnitude peaked at the new resonant frequency of 180 MHz.

Figure 17 compares the common-mode conversion coefficient with and without the improvement method, as shown by the dotted line and the solid line, respectively. The improvement ratio of the common-mode conversion coefficient at 140 MHz approximated 9 dB. Fig. 18 compares the far-field radiated emission from the TFT-LCD panel with and without the improvement method, as shown by the solid line and the thin solid line, respectively. This improvement ratio coincided with that of the far-field radiated emission from the TFT-LCD panel, in Fig. 19, which was measured in the FAC. The agreement with Fig. 19

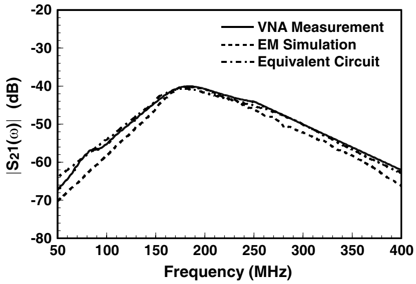

Figure 16. Comparison of common-mode conversion coefficient magnitude of the DC supply loop with shielding among VNA measurement, EM simulation and equivalent-circuit model.

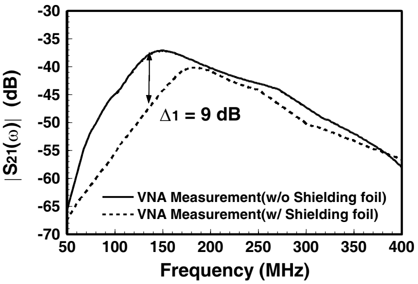

Figure 17. Comparison of measured common-mode conversion coefficient magnitude of the DC supply loop between with and without shielding foil.

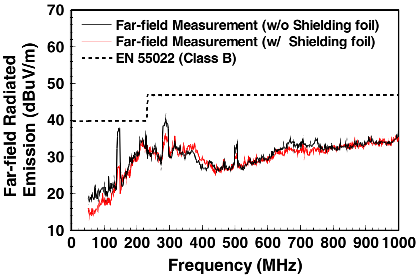

Figure 18. Comparison of measured far-field radiated emission magnitude from TFT-LCD panel between with and without shielding foil.

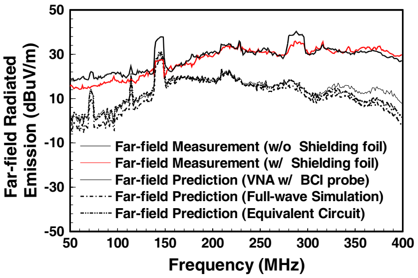

Figure 19. Comparison of improved and not improved radiated emissions from TFT-LCD panel obtained in FAC with predictions based on VNA measurement, full-wave simulation and equivalent-circuit model.

confirms the capability of the proposed technique of common-mode current measurement using a VNA with a BCI probe to predict the far-field radiated emission from a PCB.

5. CONCLUSION

This work proposes a technique for using a network analyzer with a BCI probe to measure the common-mode conversion coefficient for characterization of the common-mode radiation from a PCB. The far-field radiated emission predictions obtained by the proposed technique can be used to confirm compliance with EMC regulations. The proposed technique effectively diagnoses radiated emissions from TFT-LCD panel. For improvement, a shielding foil was used to shift the resonant frequencies of a DC supply loop on a driver PCB away from the harmonic frequencies of the clock signal from T-CON. The proposed technique was then used to assess improvements in radiated emissions from the TFT-LCD panel. The measurements obtained by the improved radiated emissions correlate well with the predictions made by common-mode conversion coefficient.

REFERENCES

1. Luo, M. and K.-M. Huang, "An extended delay-rational macromodel for electromagnetic interference analysis of mixed signal circuits," *Progress In Electromagnetics Research*, Vol. 127, 189–210, 2012.
2. Ding, T.-H., Y.-S. Li, X. Yan, and Y.-Z. Qu, "A new efficient method for calculation and suppression of simultaneous switching noise with the time-domain impedance function for high-speed circuit design," *Progress In Electromagnetics Research*, Vol. 112, 41–62, 2011.
3. Wu, B. and H. L. Lo, "Methods and designs for improving the signal integrity of vertical interconnects in high performance packaging," *Progress In Electromagnetics Research*, Vol. 123, 1–11, 2012.
4. Horng, T. S. and S. M. Wu, "Radiation from a microstrip amplifier," *IEEE Trans. Microwave Theory Tech.*, Vol. 5, 2005–2010, Aug. 2002.
5. Tremola, C., M. A. Azpurua, E. Paez, D. Ormeno, and A. Rebolledo, "An interpolation method to calibrate electromagnetic probes in semi-anechoic chambers," *Progress In Electromagnetics Research B*, Vol. 39, 355–371, 2012.
6. Li, P. and L. Jiang, "The far field transformation for the antenna modeling based on spherical electric field measurements," *Progress In Electromagnetics Research*, Vol. 123, 243–261, 2012.
7. Chen, X., "Measurements and evaluations of multi-element antennas based on limited channel samples in a reverberation chamber," *Progress In Electromagnetics Research*, Vol. 131, 45–62, 2012.
8. Staniec, K., "Evaluation of the zigbee transmission repetition

mechanism in the variably-loaded reverberation chamber," *Progress In Electromagnetics Research*, Vol. 132, 297–314, 2012.

9. Yan, W., J.-D. Xu, N.-J. Li, and W. Tan, "A novel fast near-field electromagnetic imaging method for full rotation problem," *Progress In Electromagnetics Research*, Vol. 120, 387–401, 2011.
10. Qureshi, M. A., C. H. Schmidt, and T. F. Eibert, "Adaptive sampling in multilevel plane wave based near-field far-field transformed planar near-field measurements," *Progress In Electromagnetics Research*, Vol. 126, 481–497, 2012.
11. Lotito, V., U. Sennhauser, C. V. Hafner, and G.-L. Bona, "Interaction of an asymmetric scanning near field optical microscopy probe with fluorescent molecules," *Progress In Electromagnetics Research*, Vol. 121, 281–299, 2011.
12. Liao, C.-C. and Y.-L. Lo, "Phenomenological model combining dipole-interaction signal and background effects for analyzing modulated detection in apertureless scanning near-field optical microscopy," *Progress In Electromagnetics Research*, Vol. 112, 415–440, 2011.
13. Chevallier, D., D. Baudry, and A. Louis, "Improvement of electrical near-field measurements with an electro-optic test bench," *Progress In Electromagnetics Research B*, Vol. 40, 381–398, 2012.
14. Chen, K. S., T. S. Horng, C. Y. Ho, J. M. Wu, and K. C. Peng, "Diagnosis of EMI to laptop WWAN device from TFT-LCD driver using non-contact measurement-based transfer function technique," *IEEE Int. Symp. Electromagn Compat.*, 301–304, Jul. 2010.
15. Bockelman, D. E. and W. R. Eisenstadt, "Combined differential and common-mode scattering parameters-theory and simulation," *IEEE Trans. Microwave Theory Tech.*, Vol. 43, 1530–1539, Jul. 1995.
16. Chen, C., "Examination of electronic module immunity using transfer functions," *IEEE Int. Symp. Electromagn Compat.*, 756–761, Aug. 2005.
17. Grassi, F., F. Marliani, and S. A. Pignari, "Circuit modeling of injection probes for bulk current injection," *IEEE Trans. Electromagnetic Compatibility*, Vol. 49, No. 3, 563–576, Aug. 2007.
18. Ho, C.-Y., K.-S. Chen, and T.-S. Horng, "Prediction of common-mode radiated emission from PCB using vector network analyzer with a bulk injection current probe," *Journal of Electromagnetic Waves and Applications*, Vol. 26, No. 16, 2121–2129, 2012.

19. Ho, C.-Y., K.-S. Chen, and T.-S. Horng, "Estimating radiated emission reduction from printed circuit board using vector network analyzer with a bulk current injection probe," *Progress In Electromagnetics Research*, Vol. 135, 1–16, 2013.
20. F-130-1A Injection Current Probe Characterization: Fischer Custom Communication (FCC), 2004.
21. Kim, M. W., D. W. Kim, B. S. Koo, Y. B. Kim, O. S. Choi, and N. D. Kim, "Chip level techniques for EMI reduction in LCD panels," *Proc. EMC Zurich 2009 Int. Symp. Electromagn. Compat.*, 441–444, Zurich, Switzerland, 2009.
22. Han, S. M., J.-J. Bang, C.-S. Huh, and J.-S. Choi, "A PCB noise analysis regarding EMP penetration using an electromagnetic topology method," *Progress In Electromagnetics Research*, Vol. 122, 15–27, 2012.
23. Li, Z., L. L. Liu, and C. Q. Gu, "Generalized equivalent cable bundle method for modeling EMC issues of complex cable bundle terminated in arbitrary loads," *Progress In Electromagnetics Research*, Vol. 123, 13–30, 2012.
24. Eudes, T., B. Ravelo, and A. Louis, "Transient response characterization of the high-speed interconnection RLCG-model for the signal integrity analysis," *Progress In Electromagnetics Research*, Vol. 112, 183–197, 2011.
25. Miri, M. and M. McLain, "Electromagnetic radiation from unbalanced transmission lines," *Progress In Electromagnetics Research B*, Vol. 43, 129–150, 2012.
26. Huang, Z., W. Chen, Z. Feng, K. Teshima, and K. Toyama, "Development of low cost measurement system for radiated emission evaluation," *Progress In Electromagnetics Research Letters*, Vol. 20, 55–68, 2011.
27. Paul, C. R., "A comparison of the contributions of common-mode and differential-mode currents in radiated emissions," *IEEE Trans. Electromagnetic Compatibility*, Vol. 31, No. 2, 189–193, May 1989.
28. Gomez-Revuelto, I., L. E. Garcia-Castillo, and M. Salazar-Palma, "Goal-oriented self-adaptive HP-strategies for finite element analysis of electromagnetic scattering and radiation problems," *Progress In Electromagnetics Research*, Vol. 125, 459–482, 2012.
29. Chaaban, M., K. El Khamlichi Drissi, and D. Poljak, "Analytical model for electromagnetic radiation by bare-wire structures," *Progress In Electromagnetics Research B*, Vol. 45, 395–413, 2012.